Available online at www.sciencedirect.com
SCIENCE DIRECT®
Journal of Magnetic Resonance 166 (2004) 252–261
JMR Journal of Magnetic Resonance
www.elsevier.com/locate/jmr

Magnetic resonance elastography and diffusion-weighted imaging of the sol/gel phase transition in agarose

Ingolf Sack,[a] Egbert Gedat,[a] Johannes Bernarding,[b] Gerd Buntkowsky,[c] and Jürgen Braun[a,*]

[a] *Department of Medical Informatics, Charité-University Medicine Berlin, Campus Benjamin Franklin, Hindenburgdamm 30, D-12200 Berlin, Germany*
[b] *Institute for Biometry and Medical Informatics, University Hospital of Magdeburg, Germany*
[c] *Department of Physical Chemistry, Free University of Berlin, Germany*

Received 25 July 2003; revised 24 October 2003

Abstract

The dynamics of the sol/gel phase transition in agarose was analyzed with magnetic resonance elastography (MRE) and diffusion-weighted imaging, providing complementary information on a microstructural as well as on a macroscopic spatial scale. In thermal equilibrium, the diffusion coefficient of agarose is linearly correlated with temperature, independent of the sol/gel phase transition. In larger agarose samples, the transition from the sol to the gel state was characterized by a complex position and temperature dependency of both MRE shear wave patterns and apparent diffusion coefficients (ADC). The position dependency of the temperature was experimentally found to be qualitatively similar to the behavior of the ADC maps. The dynamics of the temperature could be described with a simplified model that described the heat exchange between sol and gel compartments. The experiments supported the approach to derive temperature maps from the ADC maps by a linear relationship. The spatially resolved dynamics of the temperature maps were therefore employed to determine the elasticities. For this reason, experimental MRE data were simulated using a model of coupled harmonic oscillators. The calculated images agreed well with the experimentally observed MRE wave patterns.

Keywords: Magnetic resonance elastography; Diffusion-weighted imaging; Sol/gel phase transition; Agarose; Modulus of elasticity

1. Introduction

Magnetic resonance elastography (MRE) has been established to study in vivo the spatial distribution of the elasticity characteristics of different tissues such as mamma, muscle, and brain [1–7]. Recently, it was demonstrated that MRE can be used for the spatially resolved monitoring of the dynamics of phase transitions in thermoreversible gels [8]. Since the dynamics of the sol/gel phase transition are determined by the assemblage of complex 3-D macromolecular networks, elasticity maps can reveal the distribution and the degree of the linkage that is established between supramolecular chains in dependency of local temperatures and of the growing macromolecular network.

MRE data are accumulated in terms of phase contrast wave images showing patterns of mechanical waves [9]. These wave images need to be reconstructed for obtaining elasticity maps displaying the particular elasticity contrast. Several approaches have been reported to reconstruct MRE wave images [2,10–18]. In forward-reconstruction techniques, wave images are calculated and matched to the experiment in order to prevent inversion artifacts due to boundaries, amplitude nulls, and noisy data. Such techniques require start data for the elasticity to reconstruct in iterative procedures stepwise-refined elasticity maps until simulated and experimental data match. In [11], MRE wave images were calculated analytically employing a model of coupled harmonic oscillators (CHO) that are displaced under forced excitation.

As in most fit routines, the start values in the CHO method have to be chosen to allow the solution to

* Corresponding author. Fax: +49-30-8445-5410.
E-mail address: braun@medizin.fu-berlin.de (J. Braun).

1090-7807/$ - see front matter © 2003 Elsevier Inc. All rights reserved.
doi:10.1016/j.jmr.2003.10.020

converge toward the experimental data. Additional underlying dynamics of the examined probe, such as a muscle in different contraction states or alterations in the material properties of biopolymers in different states, lead to a time dependence of the fit parameters that determine the elasticity distribution. It may then be necessary to constrain the degrees of freedom for theoretical models that describe the dynamics of the elasticity maps. In a first approach [8] it was demonstrated that temperature-dependent Gaussian stiffness distributions were feasible to model the dynamics of sol/gel phase transitions in agarose. However, since the spatial stiffness functions were heuristically found, the underlying microscopic basis responsible for the elasticity distribution was difficult to analyze with respect to the macromolecular agarose network.

In a new approach, the time- and spatially dependent changes in the elasticity were therefore derived from diffusion-weighted imaging (DWI), which enables the quantitative determination of the diffusion of water molecules. The quantitative apparent diffusion coefficient (ADC), calculated from diffusion-weighted images, provides microstructural information on the mobility of protons in relation to temperature during phase transitions. Complex biomaterials can exhibit anisotropic and heterogeneous ADC parameters, yielding information about texture and structure. Therefore, it is preferable to find a correlation between diffusion and elasticity, which are sensitive and independent measures of the structural characteristics of materials. Since thermoreversible gels are proven to show isotropic values for ADC and elasticity, varying quantities of these parameters must be created in order to find a correlation between them. Following this line, the sol/gel phase transitions in agarose provide an ideal model system, showing heterogeneous and time-variable contrasts over a wide range of diffusion and elasticity values.

However, the complex heat distribution within the samples and the heat exchange with the environment via non-insulated surfaces have to be taken into account. To assist the interpretation of possible impacts on the diffusion coefficient of water and its relationship to the temperature, the phase transition of agarose was studied with additional experiments: (i) a pulsed field gradient (PFG) technique to resolve the temperature dependence of the ADC in agarose samples in thermal equilibrium during the phase transition; (ii) a time- and spatially resolved monitoring of the temperature during the cooling process in an extended agarose sample that was only partially in thermal equilibrium. The temperature was monitored at several positions ranging from the outer part of the sample to the core.

Analyzing the complex behavior of temperature and ADC distribution might then allow deriving temperature maps from ADC images and using this information to estimate the time-dependent spatial distribution of elasticities. The elasticity maps were verified by using them as input parameters to fit the analytic solutions of a wave equation of coupled harmonic oscillators to the experimental wave patterns.

2. Theory

2.1. Modeling the spatially dependent cooling process

To describe the temperature distribution within the sample used for the MR experiments and the heat exchange between the sol/gel compartments as well as to the environment, a simplified model is introduced (Fig. 1). The main characteristic experimental observations have to be reproduced by taking into account the time course of the temperature as measured by the thermometers at the border of the sample and in the core. The cooling process is determined by the temperature gradient between the boundaries of the different environments occurring at a rate a_1 for the cooling of the liquid state and at a rate a_2 for the cooling of the solid state. In the liquid state $(t < t_1)$, the temperature is approximately equally distributed within the sample due to the rapid and unrestricted movement of the water molecules (see Fig. 1A). Both thermometers measure the same temperature decay $T_1(t) = T_2(t)$ as the sample cools down at the rate a_1 and proportional to the temperature gradient between probe and environment (T_e).

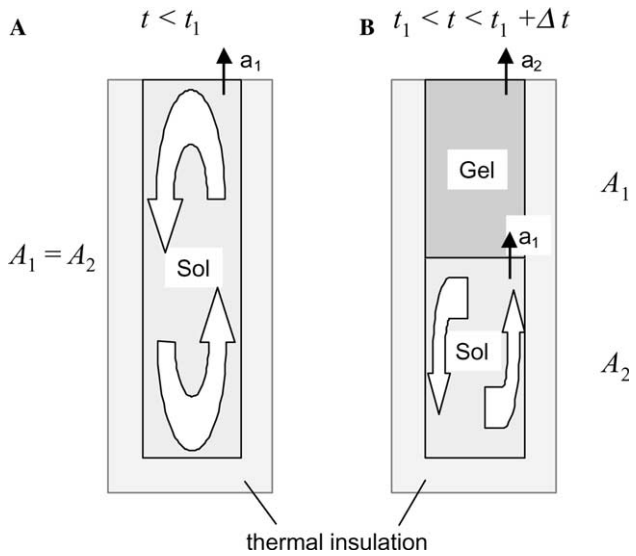

Fig. 1. Two-compartment model (A_1 and A_2) of the experimental setup for calculating the spatially dependent heat transport in agarose during sol/gel phase transitions. (A) Prior to the phase transition ($t < t_1$) the sample is fluid. Motion of the molecules leads to uniform temperature distribution. Heat exchange of the fluid part with the environment occurs at rate a_1. (B) Solidification of the outer compartment A_1 while the center of the sample (A_2) is still fluid. Heat exchange of the solid part with the environment occurs at rate a_2.

At time t_1, the outermost part (compartment A_1) solidifies and cools down at the rate a_2. As the outer solid part shields the core from the environment, the inner compartment A_2 (representing the core with only one boundary to the outer part) remains still fluid for an intermediate time Δt. During this time Δt the compartment A_1 exchanges heat at rate a_2 with the environment and at rate a_1 from the fluid part A_2 that exhibits still a higher temperature (see Fig. 1B). For $t > t_1 + \Delta t$ the core A_2 solidifies too and both compartments exchange heat at the rate a_2 while A_1 additionally loses heat at rate a_2 to the environment. This model can be expressed by the following set of coupled differential equations:

$$\frac{\mathrm{d}T_1(t)}{\mathrm{d}t} = \begin{cases} a_1(T_e - T_1(t)), \\ \quad t \leqslant t_1, \\ a_2(T_e - T_1(t)) + a_1(T_2(t) - T_1(t)), \\ \quad t_1 < t \leqslant t_1 + \Delta t, \\ a_2(T_e - T_1(t)) + a_2(T_2(t) - T_1(t)), \\ \quad t_1 + \Delta t < t, \end{cases} \tag{1}$$

$$\frac{\mathrm{d}T_2(t)}{\mathrm{d}t} = \begin{cases} a_1(T_e - T_2(t)), & t \leqslant t_1, \\ a_1(T_1(t) - T_2(t)), & t_1 < t \leqslant t_1 + \Delta t, \\ a_2(T_1(t) - T_2(t)), & t_1 + \Delta t < t. \end{cases}$$

The solutions of this coupled system of differential equations enable the evaluation of the temperature dependence over time for two distinct spatial selections. Extension to more compartments is straightforward.

2.2. Simulating wave images using coupled harmonic oscillators

The strain wave field imposed by the oscillating actuator is measured in terms of local displacements **u** in conjunction with known spatial coordinates **x**. The components of these vectors are labeled with indices, which denote the main axes of the Cartesian laboratory frame ($1 = x$, $2 = y$, $3 = z$). Using these components it is easy to define the linear, first-order terms of the strain tensor components [19]:

$$\varepsilon_{jk} = \frac{1}{2}\left(\frac{\partial u_j}{\partial x_k} + \frac{\partial u_k}{\partial y_j}\right). \tag{2}$$

In the range of deformation of dynamic MRE experiments, the stress (**σ**)–strain (**ε**) behavior of the investigated gel can be regarded as linear elastic. Thus, Hooke's law is applicable, which is given for the isotropic case as

$$\sigma_{jk} = \frac{E}{1+v}\left(\varepsilon_{jk} + \frac{v}{1-v}\varepsilon_{ll}\delta_{jk}\right), \tag{3}$$

with $\varepsilon_{ll} = \varepsilon_{jj} + \varepsilon_{kk}$ as the trace of ε and δ_{jk} as the Kronecker symbol. E and v denote Young's modulus and Poisson's ratio, respectively.

For the time-dependent displacement field the equilibrium of forces is given by:

$$f_j = \rho\frac{\partial^2 u_j}{\partial t^2} + \gamma_j\frac{\partial u_j}{\partial t} - \frac{\partial \sigma_{jk}}{\partial x_k}. \tag{4}$$

The mass term on the right-hand side incorporates the material density ρ. The spatially dependent damping term γ_j describes damping along the axis of the displacement. Substitution of Eq. (3) with Eq. (4) yields an explicit expression of the wave equation in terms of the displacement **u**:

$$f_j = \rho\frac{\partial^2 u_j}{\partial t^2} + \gamma_j\frac{\partial u_j}{\partial t} - \frac{\partial}{\partial x_i}\left(\mathbf{C}_{ijkl}\frac{\partial}{\partial x_l}\right)u_k. \tag{5}$$

The fourth-rank tensor **C** contains the elastic moduli of the system, which linearly relate stress and strain according to Hooke's law. In the 2-D case of plane stresses, **C** can be written as four second-rank tensors:

$$C_{ij11} = \begin{bmatrix} \frac{E}{1-v^2} & 0 \\ 0 & \mu \end{bmatrix}; \quad C_{ij22} = \begin{bmatrix} \mu & 0 \\ 0 & \frac{E}{1-v^2} \end{bmatrix};$$
$$C_{ij12} = \begin{bmatrix} 0 & \frac{vE}{1-v^2} \\ \mu & 0 \end{bmatrix}; \quad C_{ij21} = C_{ij12}^{\mathrm{T}}. \tag{6}$$

Here, μ denotes the shear modulus, which determines the shear wave speed of the experimentally imposed transverse waves in MR elastography:

$$\mu = \frac{E}{2(1+v)}. \tag{7}$$

Under the assumption of incompressibility, which is feasible in the case of the investigated agarose gel, the Poisson's ratio is regarded to be 0.5 and the shear modulus can be expressed as $\mu = E/3$. Thus, all elements of **C** can be derived with a known Young's modulus E.

Eq. (5) can be rearranged in a matrix algebraic expression if spatial discretization is applied. Rearranging all single displacement vectors **u** at each pixel n of the wave image in a columnwise order leads to a vector **U.** Corresponding to the order of the elements U_n (n = number of oscillators, i.e., pixels of the wave images) the finite differences in space, weighted with the coefficients of **C**, can be arranged to a band matrix **W**, which is called stiffness matrix. Assuming harmonic excitation Eq. (5) is then rewritten as

$$\mathbf{F}\cos(\varphi) = \rho\frac{\partial^2}{\partial t^2}\mathbf{U} + \mathbf{\Gamma}\frac{\partial}{\partial t}\mathbf{U} - \mathbf{W}\mathbf{U} \tag{8}$$

with **F** as the column vector containing the volumetric forces **f** at each pixel at $t = 0$. The excitation phase

$$\varphi = \omega t, \tag{9}$$

is determined by the excitation frequency ω of the MRE experiment. The damping term **Γ** in Eq. (8) is a matrix containing diagonal elements of the position-dependent damping γ_j of each pixel corresponding to U_n and zeros

otherwise. The steady-state solution of Eq. (8) is found with [11]:

$$\mathbf{U}(\varphi) = \left[\mathbf{W} - \rho\omega^2 + \omega^2\boldsymbol{\Gamma}(\mathbf{W} - \rho\omega^2)^{-1}\boldsymbol{\Gamma}\right]^{-1} \cdot \mathbf{F}\cos(\varphi) + \omega(\mathbf{W} - \rho\omega^2)^{-1}\boldsymbol{\Gamma}\left[\mathbf{W} - \rho\omega^2 + \omega^2\boldsymbol{\Gamma}(\mathbf{W} - \rho\omega^2)^{-1}\boldsymbol{\Gamma}\right]^{-1} \cdot \mathbf{F}\sin(\varphi). \quad (10)$$

Rearrangement of $\mathbf{U}$ yields two wave images for the case of 2D-CHO calculations: one for all u_1 and one for all u_2 components of $\mathbf{u}$ at each pixel. Restricted to the 2-D case, the wave images are labeled $\mathbf{U}_x$ and $\mathbf{U}_y$ corresponding to the displacement along the x- and y-axes of the lab frame.

Both components of the displacement show different wave speeds corresponding to the propagation direction with respect to $\mathbf{F}$. In our experiment, where the shear wave deflection is encoded perpendicularly to the image plane, the recorded waves are determined by the transversal shear wave speed:

$$c = \sqrt{\frac{\mu}{\rho}}. \quad (11)$$

In the plane stress scenario, the initial displacement $\mathbf{F}$ can be applied along the x-direction at the position of the transducer plate. For this case, the x-deflection image $\mathbf{U}_x$ reflects the part of the waves that travel from the top of the phantom down to the bottom at wave speed c.

2.3. Correlation of stiffness and temperature maps

To gain information about the temperature-dependent distribution of the shear elasticity used for the simulation of wave patterns, reasonable start values of the stiffness have to be assumed. In [8] it was shown that the shear elasticity increases from 0 in fluid parts to a maximum value $E_{\max}$ determined by the final temperature of the solid parts of the sample. To derive information on the pixelwise temperature distribution within the sample, ADC maps may be used, as it is well known that diffusion is very sensitive to temperature changes. As mentioned above, an increasing shear modulus corresponds to decreasing temperature. While the exact functional dependence between ADC and temperature requires additional information, it may be assumed in first approximation, that the elasticity increases linearly with decreasing temperature where the temperature maps $\mathbf{T}(t)$ have yet to be deduced from the corresponding images of the ADC values. The time course $\mathbf{E}(t)$ of the elasticity images can be described using scaled temperature maps such as

$$\mathbf{E}(t) = E_{\max}\left(1 - \frac{\mathbf{T}(t) - T_e}{T(t_1) - T_e}\right). \quad (12)$$

with T_e as the environment temperature and $T(t_1)$ as the temperature where the solidification is first observed (Eq. (1)). T_e and $T(t_1)$ are used as thresholds to scale the temperature contrast:

$$T_e < \mathbf{T}(t) < T(t_1). \quad (13)$$

The spatial distribution of $\mathbf{E}(t)$, i.e., the Young's modulus at a given time during the cooling process, as well as of the temperature can be represented as images. The parameter $E_{\max}$ in Eq. (12) reflects the global maximum value of the Young's modulus in all elasticity images of the complete series. If therefore $E_{\max}$ is determined once for the fully solidified gel, the position dependency of $\mathbf{E}(t)$ relies solely on the scaled temperature distribution used as input for the elasticity matrix.

3. Experimental methods

3.1. PFG diffusion measurements

The pulsed field gradient (PFG) NMR measurements were carried out on a Bruker MSL spectrometer (Bruker, Rheinstetten, Germany) equipped with a superconducting Oxford 300/89 magnet (Oxford Instruments, Cambridge, UK), a Doty Scientific 5 mm z-gradient probe (Doty Scientific, Columbia, SC, USA) for main field gradients up to 10 T/m, and a Techron gradient amplifier 7790 (Techron, Elkhart, IN, USA). The diffusion measurements were carried out using a stimulated echo pulse sequence with three $\pi/2$-RF pulses and two equipolar gradients after the first and the third RF pulse. The separation of the first two RF pulses was $\tau_1 = 20$ ms, and the separation of the second and the third RF pulse was $\tau_2 = 400$ ms. The $\pi/2$-pulse length was $t_{\pi/2} = 3.5\,\mu$s. The gradient strength applied was $G = 0.545$ T/m. The gradient pulse length was varied from $1\,\mu\text{s} \leqslant \delta \leqslant 600\,\mu\text{s}$ in 13 steps in arbitrary order. All other NMR parameters were kept constant. The agarose (1.5 wt%) was filled into a tube with an inner diameter of 4 mm and a length of 15 mm. The tube was closed at both ends with Teflon to minimize uncontrolled cooling. The temperature was controlled using room temperature air flow that was heated by a PC-based temperature controller (Doty Scientific). The measurements were performed on the cooling branch of the heat cycle, starting at 50 °C in steps of 5 °C down to 25 °C. For comparison of the ongoing crosslinking of the network during gelation, the diffusion coefficients of both pure water and agarose were measured. Data were calibrated to reference data of water [20] by using the H_2O measurement.

3.2. Spatially resolved imaging of the phase transition

The spatially resolved dynamics of the sol/gel phase transition was studied on a 1.5% agarose sample (22.5 g agarose, Sigma, solved in 1.5 L water heated to 95 °C).

The experimental observations were achieved over 223 min covering a temperature range from 49 °C down to 28 °C, wherein the sol/gel phase transition of agarose was completed for the whole sample. For MRI observations, liquid agarose at a temperature of 65 °C was filled in a double-wall Plexiglas container that was placed inside a standard quadrature head coil of a 1.5 T tomograph (Siemens Magnetom Vision, Siemens Erlangen, Germany). The upper side of the gel sample was kept open to favor the cooling process from the top. The transducer plate necessary for mechanical excitation of the sample was immersed from the top to a depth of 5 mm into the liquid agarose to account for the shrinking volume during gel cooling. To monitor the phase transition, three transversal slices of 5 mm thickness with an interslice distance of 10 mm were recorded. Both MRE and DWI were performed successively for each sampling time with a temporal resolution between 3 and 15 min depending on the dynamics of the phase transition in the sample.

3.3. Diffusion-weighted imaging

Diffusion-weighted images were acquired using a self-developed echo planar imaging (EPI) acquisition technique [21] (TR = 2000 ms, TE = 118 ms, field of view 220 mm, matrix size 96×128, quantity of diffusion weighting $b = 0$, 232, 511, 736, and 1001 s/mm^2). The acquisition time for a complete set of diffusion-weighted images (five images per slice) was 10 s. The diffusion-gradient orientation was set from left to right for the chosen axial slice orientation. The apparent diffusion coefficients (ADC) were calculated for each pixel by fitting the logarithm of the signal intensity over the b-values with a straight function [22]. The slope of the straight line represents the ADC for the particular pixel. The results for all pixels are displayed in terms of an image, the so-called ADC map. As EPI images usually suffer from geometrical distortions, ADC maps were registered to the gradient echo-based elasticity maps using a polynomial registration method supplied with the image processing toolbox for Matlab (R13, The MathWorks, Natick, MA, USA).

3.4. MR elastography measurements

For MR elastography, a self-developed gradient echo-based (FLASH) sequence [6] was used (TR = 60 ms, TE = 22 ms, field of view = 220 mm, matrix size 256×256 pixels, acquisition time 16 s per image). Mechanical excitation was performed with a electromechanical actuator [23] fed with 200 Hz sinusoidal AC. The wave generator was triggered at the beginning of each TR from the MR scanner. To ensure steady-state oscillations, a time delay between trigger and RF excitation pulse allowed four to five oscillations before a sinusoidal motion-encoding gradient was applied [9]. Two wave images were recorded for each slice with a relative phase shift of 180° between mechanical excitation and motion-encoding gradients. Subtraction of both images as usually performed in phase contrast techniques enhances the SNR for the oscillatory motion while simultaneously reducing apparatus influences.

3.5. Measurement and data analysis of temperature distribution during the phase transition

To correlate the ADC with the temperature distribution within the sample, the temperature was determined at five different points within the Plexiglas container already used for the MRE experiments. Thermometers were placed between center and outer regions of a liquid gel sample (agarose prepared identically to the MRE investigations). The temperature decay curves of the solidifying agarose were observed over 682 min at increments of 5 and 10 min. The outer- and innermost curves were used to fit to the solution of the system of coupled differential equations (Eq. (1)). The system was solved numerically (Maple 7, Waterloo Maple, Waterloo, Ont., Canada) using the provided finite difference scheme based on the Runge–Kutta Fehlberg method with an accuracy to the fifth order. Step size was 2.5 min; 256 time points were calculated.

3.6. CHO wave simulations

Temperature images calculated from ADC maps were converted to elasticity images $\mathbf{E}(t)$ using Eq. (12). From the PFG measurements, we assumed a linear relationship between ADC and temperature. The temperature where the phase transition could be observed first in the outermost compartment was assigned to a threshold $T(t_1)$ to exclude the sol state of the gel from the data analyses (see Eq. (13)). T_e was derived from the minimum temperature of all temperature images (24 °C room temperature).

The simulated elasticity images $\mathbf{E}(t)$ were matched to the experimental wave images by the following procedure. Variation of E_{max} in Eq. (12) yielded variable elements of the elasticity tensor $\mathbf{C}$ (Eq. (6)). Then, $\mathbf{C}$ was used to generate the stiffness matrix $\mathbf{W}$ for solving the wave equation (Eq. (10)) and a complete series of wave images was calculated. The quantity of E_{max} was determined by fitting the wave image acquired at 28 °C where the gel was completely solidified. To match the data, the profile of the central column in the calculated image was fitted by minimizing the standard deviation to the central column in the experimental image. Isotropic damping [8] was applied homogeneously over the whole oscillator matrix, with higher values at the edges to avoid reflections of the waves at the geometrical boundaries that could not be observed in the experi-

ment. $\mathbf{F}_x$, the x-component of the excitation force $\mathbf{F}$ was derived from the position of the transducer plate, which is visible at the top of the MRE images. Since pure transverse excitation was assumed, all elements of $\mathbf{F}_y$ were set to zero. Using the once-adjusted elasticity coefficient $E_{\max}$, all wave images $\mathbf{U}_x(t)$ of the entire phase transition were automatically calculated. The calculations were performed using Matlab on a Pentium 4 computer. Standard wave simulations of image matrices with a size of 100×100 pixels were achieved within 1 s.

4. Results

4.1. Diffusion measurements

The temperature dependence of the ADC was determined for H_2O and agarose in a small sample using PFG measurements (Fig. 2). Both samples exhibit a linear temperature dependence in the range between 50 and 25 °C with a similar slope of $60 \pm 3\,\mu m/s^2/K$. At 25 °C, water had a diffusion coefficient of $2276 \pm 108\,\mu m^2/s$ while the agarose sample had a somewhat reduced diffusion coefficient of $2188 \pm 96\,\mu m^2/s$.

No significant deviation from the linearity is seen in the temperature range covering the phase transition (around 39 °C).

4.2. MR imaging of the phase transition

The time course of the spatial distribution of the elasticity during the solidification process as monitored by MR elastography is displayed in the upper row of Fig. 3. The image rows are sorted from left to right by increasing time and decreasing temperature. The phase transition from the liquid sol state to the solid gel state is already visible when comparing the wave patterns along the row. While fluid parts show no transverse waves, beginning gelation leads to regions with initially small wavelengths, which increase with progressing solidification. The completed solidification, which yields nearly homogeneous elasticity, is demarcated at low temperatures (image to the right) by parallel waves throughout the object.

The spatially resolved distribution of the ADC during the phase transition is depicted in the second row. The gray scale of these images was derived from the ADC maps calculated from DWI measurements. To exclude the liquid state where the elasticity modulus is not defined, the data analyses were limited to temperatures between 39 and 25 °C.

The ADC gradient corresponding to the temperature within the probe as depicted by the gray values in the image series of row 2 declines during cooling. The ADC distribution shows a bubble-like structure that gives information about the change of phase boundaries during gelation. The circumference of this structure shrinks with ongoing solidification and falling temperatures. The local effect is better visualized by plotting the change of the ADC (Fig. 4) for five individual locations marked in the left ADC map in Fig. 3. The area of each region was approximately $25\,mm^2$. While in the beginning the ADC drops at similar rates for the inner and outer points, a branching of the curves can be observed at the time when the outer parts start to solidify. Instead of dropping further, the temperature in the inner parts stays almost constant for an intermediate time Δt until finally the temperature also decreases and converges with the outermost temperature.

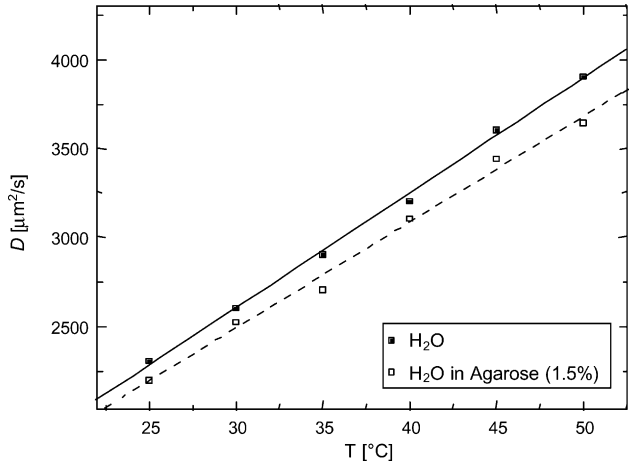

Fig. 2. PFG measurements of the diffusion coefficient of water (■) and water in agarose (1.5%) (□). The correlation between the diffusion coefficient of both water and water in agarose was found to be linear in the investigated temperature range between 25 and 50 °C. No deviations from linearity due to the gelation and the increasing crosslinking of the agarose network could be observed.

4.3. Temperature measurements

The correlation of the ADC with temperature was elucidated by directly determining the temperature at several different positions. Representative courses of the temperature at the central and the outermost positions are displayed in Fig. 5, exhibiting similar behavior to the experimental ADC data (Fig. 4). In the initial fluid state, both positions depict identical monoexponential decays. The solidification of the outer part and the consecutive splitting into a fluid and a solid compartment are depicted by the branching of the curve into two curves with non-monoexponential characteristics. Fitting the numerical solution (solid lines) of the simplified two-compartment models (Eq. (1)) to these data reproduced the qualitative behavior of the curves. The fit parameters were $a_1 = 1/(130 \pm 5)\,min^{-1}$, $a_2 = 1/(75 \pm 5)\,min^{-1}$, $t_1 = 120 \pm 2\,min$, and $\Delta t = 60 \pm 2$. Corresponding temperatures $T_1(t_1) = T_2(t_1)$ are 40 and 39 °C, respectively, with a tolerance of ±1 °C. Initial temperature and environment temperature were 65 and 24 °C, respectively.

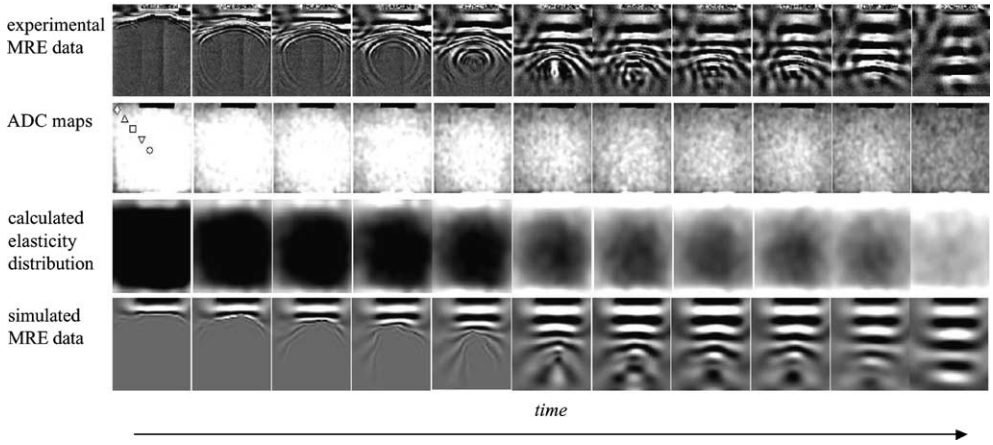

Fig. 3. Time-resolved series of MRE wave images (top row), ADC maps calculated from DWI measurements (second row), scaled elasticity maps (third row), which were used as input for the CHO wave image simulations (bottom row). Experimental MRE and DWI images were accumulated for the cooling agarose sample in a temperature range from 48 °C down to 28 °C. The selected images correspond to temperatures of T (°C) = 35.0, 33.5, 33.0, 32.5, 31.5, 30.8, 30.6, 30.4, 30.2, 29.8, and 28.0 (from left to right). The positions marked in the first image of the second row indicate selected positions used for the visualization of the temporal evolution of ADC and the Young's modulus in Figs. 4 and 6. The crosswise appearance of waves close to the excitation plate (upper part of the sample) may be due to reflections.

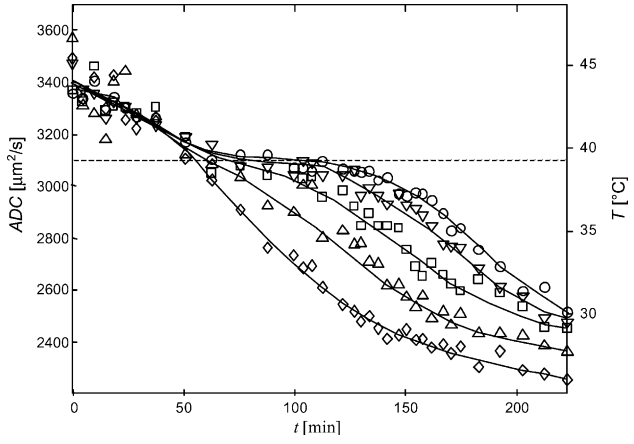

Fig. 4. Temporal evolution of the ADC for selected positions marked in Fig. 3. The lowest curve (◇) corresponds to the outermost, the upper curve (○) to the central position. The dotted line corresponds to the transition from sol to gel and indicates the upper threshold (39 °C) for scaling the temperature range according to Eq. (12). The temperature (right scale) was calculated using the PFG measurements (Fig. 2). See text for further details.

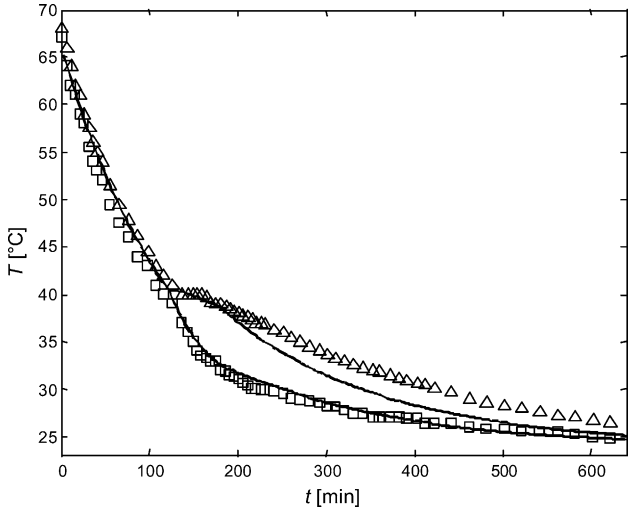

Fig. 5. Results for the cooling process of agarose without tempering. The temperature was monitored in steps of 3–10 min according to the dynamics of the cooling at a central position (Δ) and at a position in an upper edge close the surface (□) of the gel (1.5% agarose, sample volume: 1.5 L). Identical conditions were chosen to those of the setup in MRI measurements. In the temperature range between 68 and 40 °C, the system can be described by a monoexponential temperature decay. While for more peripheral positions a fast cooling rate is observable, the inner positions keep the heat for a longer time. The cooling rate for the inner liquid compartment is decreased by an additional thermal insulation of the outer solidified regions. The solid lines show a simulation of the heat exchange and the cooling for the proposed two-compartment model. A good agreement between the model and the experiments is visible.

4.4. CHO calculations

A linear relationship between ADC and temperature may be assumed from the results of the diffusion and temperature measurements, allowing the generation of elasticity maps $E(t)$ for the CHO reconstruction according to Eq. (12) (Fig. 3, third row). For five positions according to the markers in the second row of Fig. 3, the time course of the Young's modulus during the cooling process is plotted in Fig. 6. Here, the elasticity increases with time and depends on the position of the center of the phantom towards its boundaries. This reveals directly the spatially and time-resolved progress of phase transition in terms of elasticity.

Complete elasticity maps were generated and used as input for the CHO simulations. The maximum global Young's modulus was found to be 99 ± 9 kPa. The

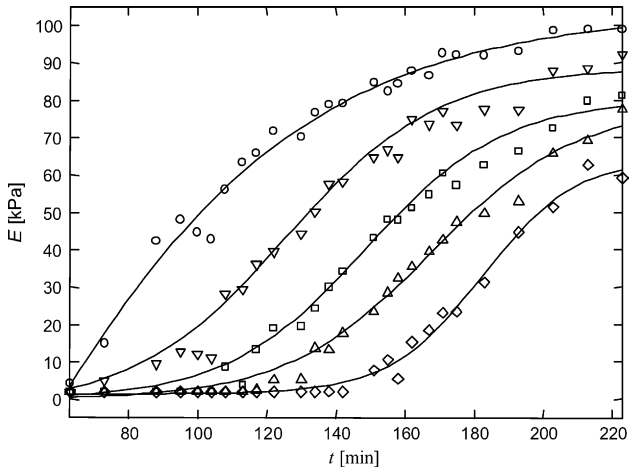

Fig. 6. Evolution of the Young's modulus E versus time under the assumption of a linear elastic incompressible medium revealed by CHO wave simulations. The symbols of the graphs correspond to the positions indicated in Fig. 3. Due to the temperature threshold, which was set to 39 °C, the first points for the innermost regions are truncated. In order to avoid experimentally not observable reflections, the minimum value for the Young's modulus was set to 1.5% of $E_{\max}$. See text for further details.

minimum elasticity was set to a finite small value of approximately $1.5 \pm 0.5\%$ of $E_{\max}$ in order to avoid reflections of the waves. Assuming the condition of incompressibility, the shear modulus $\mu_{\max}$ could be derived from $E_{\max}$ according to Hooke's law to 33 ± 3 kPa. This value corresponds to a shear wave propagation speed of 5.7 ± 0.4 m/s.

To finally match the simulations with the experimental waves, the relative phase of the simulated wave images was varied. Best agreement with the phase of the experimental wave images was found at $\varphi = 270°$. The simulated CHO wave images $\mathbf{U}_x(270°, t)$ are displayed in the bottom row of Fig. 3.

5. Discussion

The results show that diffusion-weighted imaging can be employed to support MR elastography wave simulations for exploring phase transitions in agarose gel. However, the complex spatially and time-dependent behavior of the ADC required an analysis of how temperature, ADC and elasticity are connected in larger agarose gel phantoms during a phase transition.

The PFG experiments proved clearly that for small one-compartment samples in thermal equilibrium, the correlation between the diffusion coefficient of water in agarose depends linearly on the temperature, independent of the sol/gel phase transition. Interestingly, the diffusion in the gel is somewhat smaller than water but is not additionally influenced by the increasing crosslinking during gelation.

The complex temperature dependence within the large non-tempered agarose probe could be qualitatively well described by the proposed simplified two-compartment model. In good agreement with experimental data, the branching of the temperature decay and the deviation from monoexponentiality occurs when outer areas of the phantom start to solidify. The characteristics of these discontinuities depend on the position at which the temperature was monitored within the investigated object.

It was found that in the vicinity of the outer boundaries of the gel phantom, the temperature decreases faster with beginning solidification. The faster decay is caused by increased heat transport due to an initially steeper temperature gradient in regions close to the wall of the container. Additionally, the progressing solidification starting from the outer boundaries causes a shielding of the heat in the inner liquid compartment. Therefore, the inner temperature decays at a lower rate than that of the outer compartment. Thus, images of the temperature distribution can display the boundaries of the sol/gel phase transition due to: (i) the thermal insulation of central liquid parts and (ii) the elevated heat transport within the solidified agarose in the outer parts of the gel phantom.

The simple two-compartment model predicts an equal decay rate for inner and outer compartments after $t_1 + \Delta t$, i.e., after completed solidification. It can be realized that the experimental data (Fig. 5) display a deviation from this prediction although the main features were well met. The experimental temperature threshold of 39 °C for the solidification of the outer parts in Fig. 4 is the mean of the fitted transition temperatures of 40 ± 1 °C for the outer parts and 38 ± 1 °C for the core. The small splitting of the fitted transition temperatures is a side effect of the simplification modeling a solid outer and a fluid inner part simultaneously during Δt. Extending the theory to more complex heat exchange mechanisms within multiple compartments and including heat conduction in solid gel rods is expected to better fit the temperature decays in this range.

Comparing the temperature evolution (Fig. 5) with the change in ADC (Fig. 4) reveals that both parameters share the same characteristics. Although decay rates and the timing of the phase transition are not comparable due to different T_0 and T_e values, two principal ranges determined by t_1 are well observable in both graphs. In the high temperature range for $t < t_1$, the ADC contrast decreases uniformly for the liquid gel without spatial differences, similarly to the temperature decays in Fig. 5. After t_1 the ADC and temperature contrast evolve position dependently. MRI techniques thus allow a spatially resolved monitoring of the phase boundaries. The time resolution achieved for a complete series of MRE wave images and DWI for three slices was 3 min. Compared to the large sample volume and the slow

cooling process for each time point, thermal equilibrium conditions in volumes corresponding to the voxel resolution can be assumed.

The ADC-derived temperature maps allowed us to exploit the spatial distribution of the phase transition and to include this information in the elasticity maps used for the CHO simulation.

Conversion of the ADC-derived temperature maps to elasticity images required the application of inversion, scaling, and restriction to a temperature range between beginning and completed gelation according to Eq. (12). This approach was justified by the successful simulation of experimental wave images using the CHO calculations. Since the geometrical information about phase boundaries was preserved in the applied linear transformation of the temperature maps to elasticity maps, only a single scaling factor was necessary to match all simulated wave images to the experimental data.

Besides the known temperatures of the environment and of the position of the phase transition, the applied transformation rule is based on an adjustment of Young's modulus for simulated images to the experimental data. Since the comparison of experiment and simulation, because of the simplicity of the observed wave patterns, can be achieved easiest on the fully solidified phantom, the maximum elasticity ($E_{\max}$) was chosen as parameter to calibrate once the elasticity matrix needed as input for the CHO calculations. Following this strategy, the reconstruction of a complete series of wave images of the MRE phase transition experiment is as straightforward as the simulation of a single homogeneous wave image.

The feasibility of this approach was demonstrated in Fig. 3. The good agreement of CHO wave image simulations based on the scaled temperature maps with experimental data demonstrates the value of supplementary information for simplifying complex reconstruction tasks. This is especially important in MR elastography where the elasticity maps possess a high degree of freedom. The number of possible combinations of elasticity parameters increases with the spatial resolution of the experimental wave images. Complementary image information that is not directly related to mechanical properties characterizing the network status of gelating agarose can be interpreted in terms of phase transitions. Although this was demonstrated using ADC maps calculated from DWI, possible alternatives could include other temperature-sensitive data acquisition schemes [24,25].

6. Conclusion

It was shown that temperature and elasticity provide complementary measures for the degree of the macromolecular network linkage in agarose gels. Both quantities were monitored time- and spatially resolved during sol/gel phase transition in agarose. It was found that in thermal equilibrium the diffusion is linearly dependent on the temperature in agarose gels even during a phase transition. For more complex experimental setups without tempering the sample and establishing equilibrium conditions for the measurements, the temperature decreases with different local decay rates that could be qualitatively explained by a simplified two-compartment model. The time-resolved temperature distribution in the range between 39 and 28 °C was scaled to the Young's modulus. The spatially resolved elasticities increased from nearly zero in the liquid sol state to a limit value of the maximum elasticity determined by the completely solidified gel. The geometry of the phase transition boundaries explored by the temperature distribution calculated from ADC maps could in this way be introduced as input for the reconstruction of MR elastography wave images with the CHO approach after linear scaling. Best fit was achieved using an elasticity scale between 1.5 ± 0.5 and 99 ± 9 kPa for Young's modulus, which was directly related to the geometry of the temperature distribution.

The presented approach uses only image-derived experimental data for the generation of time- and spatially resolved elasticity maps instead of a priori assumptions. This enables the building of models that are based on underlying physical principles rather than heuristic assumptions about the dynamics of elasticity.

Since alterations such as growing or degradation of macromolecular or cellular networks are most sensitively observable in terms of local elasticities, MR elastography can play an important role in understanding effects not only in biomechanics and medicine but also in materials science.

Acknowledgments

Support from the Ernst Schering Research Foundation, Berlin, and the Fonds der Chemischen Industrie, Frankfurt, is gratefully acknowledged. We thank Ms. Jean Pietrowicz for carefully proofreading the manuscript.

References

[1] S.A. Kruse, M.A. Dresner, P.J. Rossman, J.P. Felmlee, C.R. Jack, R.L. Ehman, Palpation of the brain using magnetic resonance elastography, in: Proceedings of the Seventh Conference of the International Society of Magnetic Resonance in Medicine, 1999, p. 258.

[2] R. Sinkus, J. Lorenzen, D. Schrader, M. Lorenzen, M. Dargatz, D. Holz, High-resolution tensor MR elastography for breast tumour detection, Phys. Med. Biol. 45 (2000) 1649–1664.

[3] D.B. Plewes, J. Bishop, A. Samani, J. Sciarretta, Visualization and quantification of breast cancer biomechanical properties with magnetic resonance elastography, Phys. Med. Biol. 45 (2000) 1591–1610.
[4] S.A. Kruse, J.A. Smith, A.J. Lawrence, M.A. Dresner, A. Manduca, J.F. Greenleaf, R.L. Ehman, Tissue characterization using magnetic resonance elastography: preliminary results, Phys. Med. Biol. 45 (2000) 1579–1590.
[5] M.A. Dresner, G.H. Rose, P.J. Rossman, R. Muthupillai, A. Manduca, R.L. Ehman, Magnetic resonance elastography of skeletal muscle, J. Magn. Reson. Imaging 13 (2001) 269–276.
[6] I. Sack, J. Bernarding, J. Braun, Analysis of wave patterns in MR elastography of skeletal muscle using coupled harmonic oscillator simulations, Magn. Reson. Imaging 20 (2002) 95–104.
[7] J. Braun, J. Bernarding, T. Tolxdorff, I. Sack, In vivo magnetic resonance elastography of the human brain using ultrafast acquisition techniques, in: Proceedings of the 10th Conference of the International Society of Magnetic Resonance in Medicine, 2002, p. 2597.
[8] I. Sack, G. Buntkowsky, J. Bernarding, J. Braun, Magnetic resonance elastography: a method for the noninvasive and spatially resolved observation of phase transitions in gels, J. Am. Chem. Soc. 123 (2001) 11087–11088.
[9] R. Muthupillai, D.J. Lomas, P.J. Rossman, J.F. Greenleaf, A. Manduca, R.L. Ehman, Magnetic resonance elastography by direct visualization of propagating acoustic strain waves, Science 269 (1995) 1854–1857.
[10] J. Bishop, A. Samani, J. Sciarretta, D. Plewes, Two-dimensional MR elastrography with linear inversion reconstruction: methodology and noise analysis, Phys. Med. Biol. 45 (2000) 2081–2091.
[11] J. Braun, G. Buntkowsky, J. Bernarding, T. Tolxdorff, I. Sack, Simulation and analysis of magnetic resonance elastography wave images using coupled harmonic oscillators and Gaussian local frequency estimation, Magn. Reson. Imaging 19 (2001) 703–713.
[12] A. Manduca, R. Muthupillai, P.J. Rossman, J.F. Greenleaf, R.L. Ehman, Image processing for magnetic resonance elastography, in: M.H. Loew, K.M. Hanson (Eds.), Proceedings of the SPIE's International Symposium on Medical Imaging, San Diego, 1996, pp. 616–623.
[13] A. Manduca, T.E. Oliphant, M.A. Dresner, J.L. Mahowald, S.A. Kruse, E. Amromin, J.P. Felmlee, J.F. Greenleaf, R.L. Ehman, Magnetic resonance elastography: non-invasive mapping of tissue elasticity, Med. Image Anal. 5 (2001) 237–254.
[14] T.E. Oliphant, A. Manduca, R.L. Ehman, J.F. Greenleaf, Complex-valued stiffness reconstruction for magnetic resonance elastography by algebraic inversion of the differential equation, Magn. Reson. Med. 45 (2001) 299–310.
[15] A.J. Romano, J.J. Shirron, J.A. Bucaro, On the noninvasive determination of material parameters from a knowledge of elastic displacements: theory and numerical simulation, IEEE Trans. Ultrason. Ferroelectr. Freq. Control 45 (1998) 751–759.
[16] I. Sack, G. Buntkowsky, J. Bernarding, E. Gedat, T. Tolxdorff, J. Braun, Reconstruction of MR elastography wave images by inversion of the coupled harmonic oscillator equation, in: Proceedings of the 19th Meeting of the European Society of Magnetic Resonance in Med. Biol., 2002, p. 19.
[17] E. Van Houten, M. Miga, J. Weaver, F. Kennedy, K. Paulsen, Three-dimensional subzone-based reconstruction algorithm for MR elastography, Magn. Reson. Med. 45 (2001) 827–837.
[18] E.E. Van Houten, K.D. Paulsen, M.I. Miga, F.E. Kennedy, J.B. Weaver, An overlapping subzone technique for MR-based elastic property reconstruction, Magn. Reson. Med. 42 (1999) 779–786.
[19] L.D. Landau, E.M. Lifschitz, in: Theory of Elasticity, vol. 7, Pergamon Press, Oxford, 1986.
[20] M. Holz, S. Heil, Temperature-dependent self-diffusion coefficients of water and six selected molecular liquids for calibration in accurate ^{1}H NMR PFG measurements, Phys. Chem. 2 (2000) 4740–4747.
[21] J. Braun, J. Bernarding, C. Koennecke, K.J. Wolf, T. Tolxdorff, Feature-based, automated segmentation of human cerebral infarcts including diffusion-weighted imaging, Computer Methods Biomech. Biomed. Engin. 5 (2002) 411–420.
[22] J. Bernarding, J. Braun, J. Hohmann, U. Mansmann, M. Hoehn-Berlage, C. Stapf, K.J. Wolf, T. Tolxdorff, Histogram-based characterization of healthy and ischemic brain tissues using multiparametric MR imaging including apparent diffusion coefficient maps and relaxometry, Magn. Reson. Med. 43 (2000) 52–61.
[23] J. Braun, K. Braun, I. Sack, An electromagnetic actuator for generating variably oriented shear waves in MR elastography, Magn. Reson. Med. 50 (2003) 220–222.
[24] Y.C. Chung, J.L. Duerk, A. Shankaranarayanan, M. Hampke, E.M. Merkle, J.S. Lewin, Temperature measurement using echo-shifted FLASH at low field for interventional MRI, J. Magn. Reson. Imaging 9 (1999) 138–145.
[25] W. Wlodarczyk, M. Hentschel, P. Wust, R. Noeske, N. Hosten, H. Rinneberg, R. Felix, Comparison of four magnetic resonance methods for mapping small temperature changes, Phys. Med. Biol. 44 (1999) 607–624.